ACS APPLIED MATERIALS & INTERFACES

www.acsami.org

Research Article

Pinned Electrode/Electrolyte Interphase and Its Formation Origin for Sulfurized Polyacrylonitrile Cathode in Stable Lithium Batteries

Xianhui Zhang,‡ Peiyuan Gao,‡ Zhaohui Wu, Mark H. Engelhard, Xia Cao, Hao Jia, Yaobin Xu, Haodong Liu, Chongming Wang, Jun Liu, Ji-Guang Zhang, Ping Liu,* and Wu Xu*

Cite This: *ACS Appl. Mater. Interfaces* 2022, 14, 52046−52057

Read Online

ACCESS | Metrics & More | Article Recommendations | Supporting Information

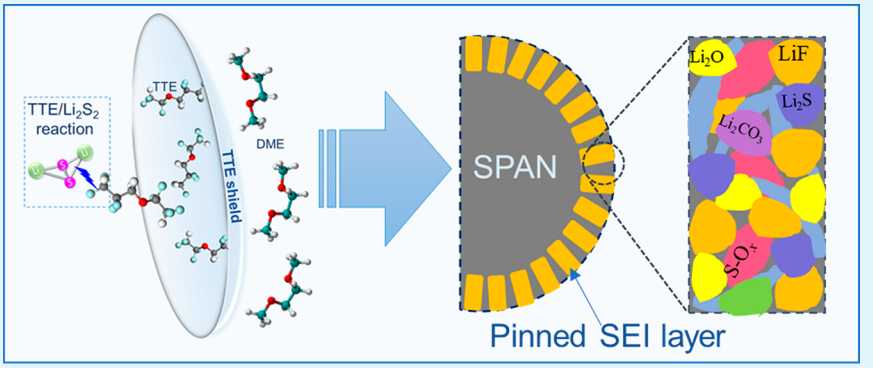

ABSTRACT: Sulfurized polyacrylonitrile (SPAN) represents one of the most promising directions for high-energy-density lithium (Li)-sulfur batteries. However, the practical application of Li||SPAN is currently limited by the insufficient chemical/electrochemical stability of electrode/electrolyte interphase (EEI). Here, a pinned EEI layer is designed for stabilizing a SPAN cathode by regulating the EEI formation mechanism in an advanced LiFSI/ether/fluorinated-ether electrolyte. Computational simulations and experimental investigations reveal that, benefiting from the nonsolvating nature, the fluorinated-ether can not only act as a protective shield to prevent the Li polysulfides dissolution but also, more importantly, endow a diffusion-controlled EEI formation process. It promotes the formation of a uniform, protective, and conductive EEI layer pinning into SPAN surface region, enabling the high loading Li||SPAN batteries with superior cycling stability, wide temperature performance, and high-rate capability. This design strategy opens an avenue for exploring advanced electrolytes for Li||SPAN batteries and guides the interface design for broad types of battery systems.

KEYWORDS: *lithium−sulfur batteries, sulfurized polyacrylonitrile, Li metal anode, high cathode loading, electrode/electrolyte interphase*

INTRODUCTION

Being known for overwhelming theoretical specific energy (2600 Wh kg^{-1}) and advantages regarding low cost, natural abundance, and environmental benignity of sulfur (S), lithium (Li)||S batteries hold particular promise to meet the increasing demand for advanced energy storage beyond state-of-the-art Li-ion batteries.[1,2] However, conventional carbon (C)/S composite cathodes for Li||S batteries face fundamental challenges originating from the insulating properties of elemental S and Li_2S, the shuttling of soluble Li polysulfides (LPSs, Li_2S_n, $2 < n \leq 8$), the reactivity of LPSs especially radical species, and the drastic volume and morphology changes of the S cathode on cycling, which result in low capacity utilization and poor cycling stability, then strongly hindering the practical applications of Li||S batteries.[3,4] As an alternative cathode for Li||S batteries, sulfurized polyacrylonitrile (SPAN) is reported to achieve significant success in mitigating LPSs shuttling due to the confinement of short molecular S units (S_n, $n \leq 4$) and the covalently bonded S atoms onto the polyacrylonitrile (PAN) heterocyclic backbones.[5,6] Moreover, the SPAN cathode exhibits negligible self-discharge and higher intrinsic electrical/ionic conductivities than elemental S.[7,8] These competitive advantages endow SPAN cathode increasing attentions worldwide as a promising cathode for alternative Li||S batteries.[9−11]

Long-term cycling stability of Li||SPAN batteries has been demonstrated in numerous studies with conventional $LiPF_6$/carbonate-based electrolytes because of their good chemical compatibility with SPAN cathodes.[12−15] However, carbonate-

Received: September 19, 2022
Accepted: November 3, 2022
Published: November 15, 2022

based electrolytes are widely acknowledged to be incompetent to protect Li metal anode, manifested by rapid capacity decay and short lifespan due to the uncontrollable Li deposition and stripping, electrolyte consumption, and continuous growth of insulating solid-electrolyte interphase (SEI) layer.[16,17] Even worse, it is revealed that in a $LiPF_6$/carbonate electrolyte, the soluble decomposition products generated on the Li metal surface can diffuse through the electrolyte to the cathode side, *i.e.*, the crossover phenomenon, leading to severely detrimental effects on cathode stability and cell performance.[18] In addition, the reported long cycle life of those Li||SPAN cells with carbonate-based electrolytes is usually realized with low S-containing electrodes (~1.0 mg cm^{-2}, cathode areal capacity loading <3.0 mg cm^{-2}).[19,20] With an increase in SPAN loading (*i.e.*, thicker cathode), LPSs crossover would be multiplied and areal current density passing through Li metal electrodes is amplified, rendering rapid capacity decay, large polarization and short lifespan.[21−23] This is supported by the significantly diminished lifespan of Li||SPAN cells with high SPAN loading compared to that with low SPAN loading (Table S1), overshadowing the advantages of carbonate-based electrolytes toward SPAN cathodes.[24,25] Therefore, it is much more stringent to develop favorable electrolytes for high loading SPAN when aiming to maximize the energy density of Li−S batteries.

To advance the practical applications of Li||SPAN batteries, it is critical to design advanced electrolyte that simultaneously satisfies the following criteria: (1) good compatibility with Li metal anode, (2) being able to stabilize SPAN cathode even with high S loading, (3) being capable of suppressing LPSs dissolution and shutting, (4) empowering the operation under challenged conditions, including high temperature (HT), low temperature (LT) and high rate. Another challenging situation in Li||SPAN is that the SPAN is quasi-polymer and microporous material, making the formation of a dense and uniform cathode/electrolyte interphase (CEI) layer on SPAN surface more difficult than on materials with single crystal, lamellar, or spherical particles.[12] Therefore, beside the above-mentioned four criteria for electrolyte optimization, the architecture of the CEI, which is often the most-overlooked, should also be carefully regulated. In recent years, ether-based electrolytes have been empirically verified to be well compatible with Li metal anodes and demonstrated the favorable effects on enhancing HT and LT performances and rate capability in Li metal batteries, Na−S batteries, Li−O_2 batteries, *etc.*, thus attracting growing attention for the application in Li||SPAN system.[26−29] However, it is reported that the solubility of Li_2S_n ($n \leq 4$) in ether electrolytes is strong enough to induce the LPSs dissolution and the shuttling effect,[30,31] prohibiting their applications in practical Li||S batteries, especially with high loading SPAN as cathodes.

Aiming to avoid the LPSs dissolution in ether-based electrolyte, a workable strategy is to isolate the ether solvents and LPSs from each other, which could be realized by reducing the amount of "free" ether solvent or build a shield between the LPSs and ether solvent. Fluorinated solvents is known to be nonsolvating or low-solvating in electrolyte, which leads to the Li^+/solvent clusters being restricted in the primary coordination shell, thus the amount of free solvent molecules will be reduced. Taking advantage of this special property, here, we introduce a fluorinated ether, 1,1,2,2-tetrafluoroethyl-2,2,3,3-tetrafluoropropyl ether (TTE), into an ether-based electrolyte of lithium bis(fluorosulfonyl)imide (LiFSI) in 1,2-dimethoxyethane (DME), with the molar ratio of 1:1.2:3 for LiFSI:DME:TTE, referring as LFSI-ether hereafter. Benefiting from the high salt/solvent ratio and the nonsolvating TTE, the design of LFSI-ether is demonstrated to be successful in eliminating LPSs dissolution. Further computational simulations and experimental investigation reveal the distinct CEI formation mechanism in LFSI-ether, which is quite different from those in previous reports. The unique CEI formation process in early cycles endowed by TTE contributes to a robust, uniform, and conductive CEI pinning inside the SPAN bulk on the surface region. Such a pinned CEI can well stabilize the SPAN cathode even with high active material loading. Subsequently, Li||SPAN cells with a high SPAN loading of ~11.0 mg cm^{-2} in LFSI-ether electrolyte exhibit much better 25 and 60 °C cycling stability, LT discharge performance and high-rate capability than those in $LiPF_6$/carbonate-based electrolyte (1.0 M $LiPF_6$ in ethylene carbonate (EC)/ethyl methyl carbonate (EMC) (3:7 by wt.) with 2 wt % vinylene carbonate (VC), hereafter referred as LPF-carbonate). This work provides inspiring guides for the rational design of advanced electrolytes for Li||SPAN batteries and pave the way to future high-energy density Li||S applications.

EXPERIMENTAL DETAILS

Electrode and Electrolyte Preparation. The SPAN material and SPAN electrode were prepared by following a similar procedure in the previous report.[27] The SPAN electrode was prepared by mixing SPAN powder, conduct carbon and CMC binder at a weight ratio of 80:10:10, and then obtained slurry was cast on Al foil. The cathode laminates were punched into disks of 1.0 cm in diameter. The electrode disks were further dried at 60 °C overnight under vacuum before use. The sulfur loading in SPAN cathode used in this study was ~11 mg cm^{-2}. Li-metal chips (diameter: 1.55 cm) were purchased from MTI Corporation. The electrolytes were prepared by dissolving LiFSI (battery grade, from Nippon Shokubai, Japan) or $LiPF_6$ (battery grade, from Gotion, Inc., USA) in the selected solvents and additive mixtures inside an MBraun glovebox filled with purified argon, where the moisture and oxygen content was less than 1 ppm. Battery grade EC, EMC, DME, and VC were ordered from Gotion and used as received. TTE (99%) was purchased from SynQuest Laboratories (USA) and dried with preactivated molecular sieves before use.

Electrochemical Tests. CR2032 coin cells (from MTI Corporation) with stainless steel negative cans and positive cans were assembled for electrochemical measurements. A piece of Li chip, a piece of polyethylene separator (1.9 cm in diameter, ordered from Asahi Kasei Hipore, Japan) and a piece of SPAN cathode disk were sandwiched together. Expect for the lean electrolyte test with 50 μm Li metal anode and 13 μL electrolyte (Figure S2) in CR2032 coin cells, the amount of electrolyte injected in each coin cell is 75 μL and the Li metal thickness are 250 μm. After being crimped into coin cells inside the argon-filled glovebox (MBraun, with H_2O < 1 ppm, O_2 < 1 ppm), the obtained cells were connected to Landt battery testers and the electrochemical performances were evaluated. The test procedure was consisted of two formation cycles at C/10 and long-term cycling performance evaluation at C/5, where 1C = 6.0 mA cm^{-2}. The voltage range of 1.0−3.0 V was applied for all charge/discharge cycles. Long-term cycling performance evaluations were conducted under selected operation temperatures of 25 and 60 °C. Electrochemical impedance spectroscopy (EIS) measurements were performed with a 1255B Solartron frequency response analyzer in combination with a 1287 Solartron electrochemical workstation. The perturbation amplitude of 5 mV within the frequency range of 10^5 to 10^{-3} Hz was applied to each cell.

Characterizations. After cycling, the cells were carefully disassembled inside the glovebox to collect the Li anodes and

https://doi.org/10.1021/acsami.2c16890
ACS Appl. Mater. Interfaces 2022, 14, 52046−52057

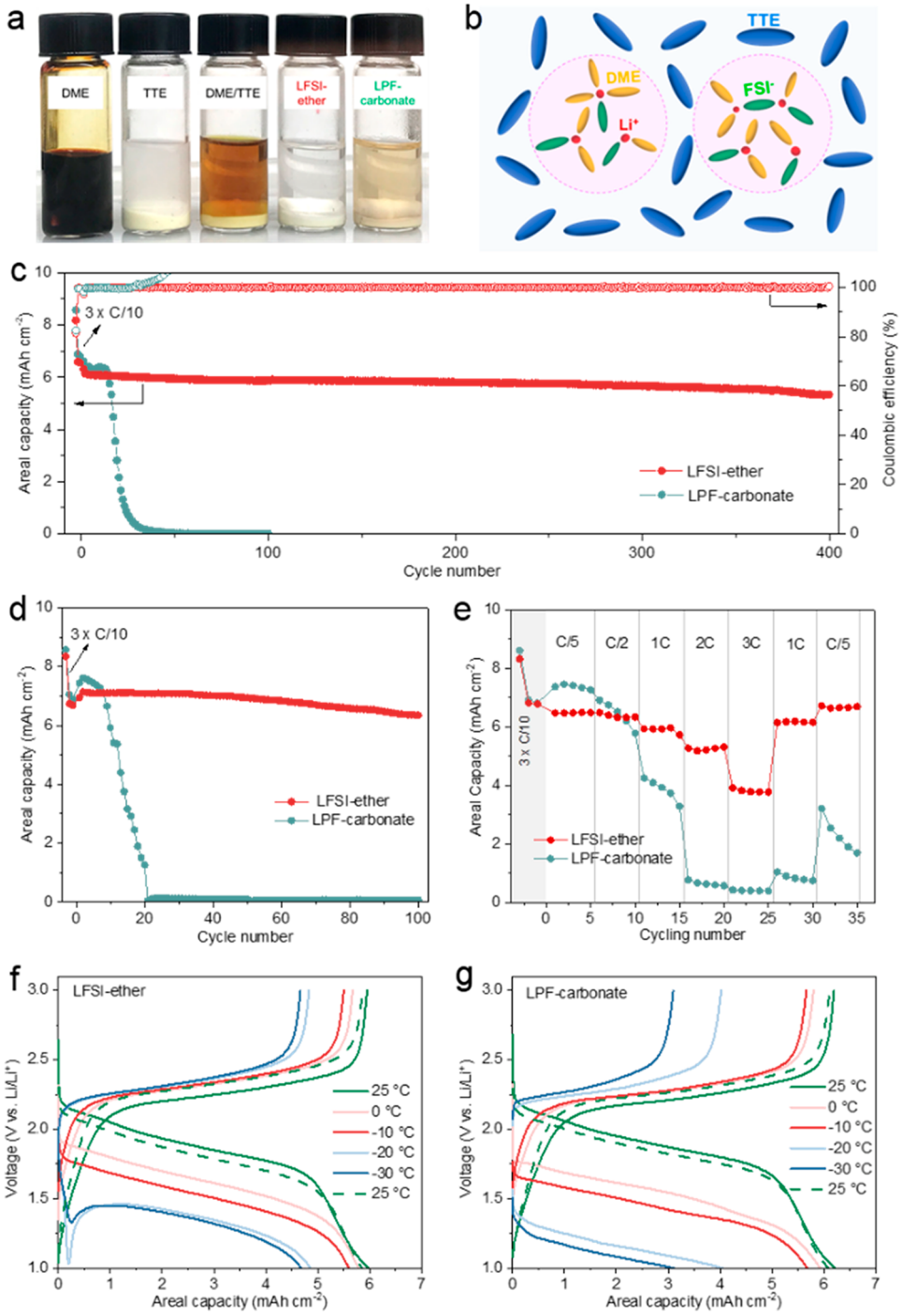

Figure 1. Electrolyte behaviors and electrochemical performances of Li||SPAN batteries in the voltage range of 1.0−3.0 V. (a) Solubility tests with 0.25 M Li_2S_6 by stirring stoichiometric amounts of Li_2S and S for 12 h in different solvents and electrolytes. (b) The scheme of the solvation structure in LFSI-ether. (c, d) Long-term cycling stability at C/5 rate under (c) 25 °C and (d) 60 °C. (e) Discharge rate capability tests under 60 °C with a constant charge rate of C/5. (f, g) Low-temperature discharge tests at C/5 with (f) LFSI-ether and (g) LPF-carbonate. The operating temperature for all charging process was 25 °C. 1C = 6.0 mA cm^{-2}.

SPAN cathodes. These cycled electrodes were rinsed with pure anhydrous solvent (EMC for the cells using LPF-carbonate and DME for the ones using LFSI-ether) to remove residual electrolyte, dried under vacuum, and then sealed in the glovebox before being transferred for scanning electron microscopy (SEM) and X-ray photoelectron spectroscopy (XPS) measurements. SEM measurements were carried out on a Helios focused ion beam SEM at an accelerating voltage of 5 kV and a current of 86 pA. The as-prepared sample was characterized by a JEOL JEM-ARM200CF spherical-aberration-corrected microscope with a convergence angle set at 20.6 mrad for imaging. XPS measurements were conducted on a Physical Electronics Quantera scanning X-ray microprobe with a focused monochromatic Al Kα X-ray (1,486.7 eV) source for excitation and a pass energy of 69.0 eV for high-energy-resolution spectra collection. All the XPS results were fitted with CasaXPS software. The binding energy was calibrated with C 1s at 284.8 eV. Shirley BG type was used for background subtraction and GL (30) line shape was used for peak fitting.

Theoretical Basis. *DFT Calculation.* Density functional theory (DFT) calculations of isolated SPAN molecules with various chemical

https://doi.org/10.1021/acsami.2c16890
ACS Appl. Mater. Interfaces 2022, 14, 52046−52057

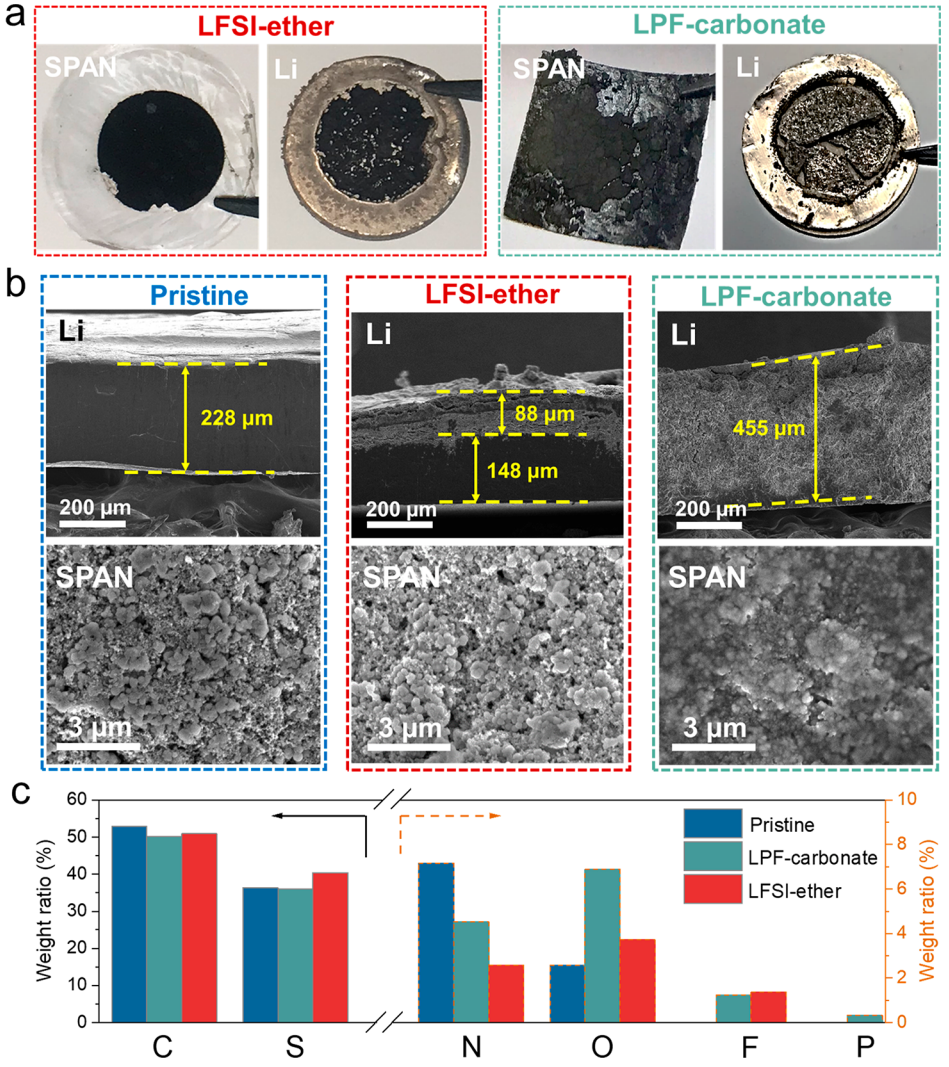

Figure 2. SPAN cathodes and Li metal anodes after 100 cycles at 25 °C in LFSI-ether and LPF-carbonate, respectively. (a) Pictures of the cycled SPAN cathodes and Li metal anodes. (b) SEM images of pristine and cycled electrodes and (c) weight ratios of the detected elements in EDS mapping.

structures were performed using the M06-2X functional with NWChem software.[32] The geometries of the molecules were optimized with 6-31G** basis. Vibrational frequencies were calculated for validation of stable configuration. An effect of implicit solvent model with dielectric properties of TTE (dielectric constant = 6.2) was included for LHCE system via COSMO model. More details are in Supporting Information.

AIMD Simulation. *Ab initio* molecular dynamics (AIMD) simulations of Li in various bulk SPAN structures during charge and discharge processing were carried out by Vienna *Ab initio* Simulation Package (VASP). Electron−ion interactions were described by the projector-augmented wave (PAW) pseudopotentials[33] with the cutoff energy of 400 eV. The exchange-correlation functional was represented using the Perdew−Burke−Ernzerhof generalized gradient approximation (GGA-PBE). The exchange-correlation functional with a Gaussian smearing width term of 0.05 eV was used. The convergence criteria for electronic self-consistent iteration was set to 1×10^{-5} eV. Long-range dispersion interaction was corrected by DFT-D3 method. To accelerate to reaction, the reaction dynamics of Li in SPAN during charge−discharge processes were investigated in the canonical ensemble at 330 K. The constant temperature of the AIMD simulation systems was controlled using the Nosé thermostat method with a Nosé-mass parameter of 0.1. These initial geometry structures were first minimized with molecular mechanics method. Then, it was equilibrated by 5 ns classical MD simulation with OPLS-AA force field. The final configuration was imported into AIMD simulation as the initial configuration. The time step of 1 fs was used in AIMD simulations. The gamma point sampling was used for the Brillouin zone. The simulation time in charge and discharge processes was 20 ps, respectively. The interface models were built to investigate the reactions between solvent (DME), diluent (TTE), anion (FSI), and Li_2S_2, respectively. The Li_2S_2 (100) facet was selected and the slab models with eight layers were used after the convergence test. Six solvent diluent/anion were added on the surface. The bottom six layers were fixed in AIMD simulation. The dipole correction was applied for all the surface systems. The thickness of vacuum at z direction was set to be 16 Å to avoid interactions between the atoms and their periodical images. The reaction dynamics between Li_2S_2 and other species were investigated in the canonical ensemble at 298 K, respectively. The constant temperature of the AIMD simulation systems was controlled using the Nosé thermostat method with a Nosé-mass parameter of 0.1. The systems were relaxed for 200 steps first. The time step is 0.5 fs. Then 4 ps simulation was performed for each system. More details are in Supporting Information.

RESULTS AND DISCUSSION

Cell Performances with High Loading SPAN Cathodes. First, the chemical compatibilities of LFSI-ether and

https://doi.org/10.1021/acsami.2c16890
ACS Appl. Mater. Interfaces 2022, 14, 52046−52057

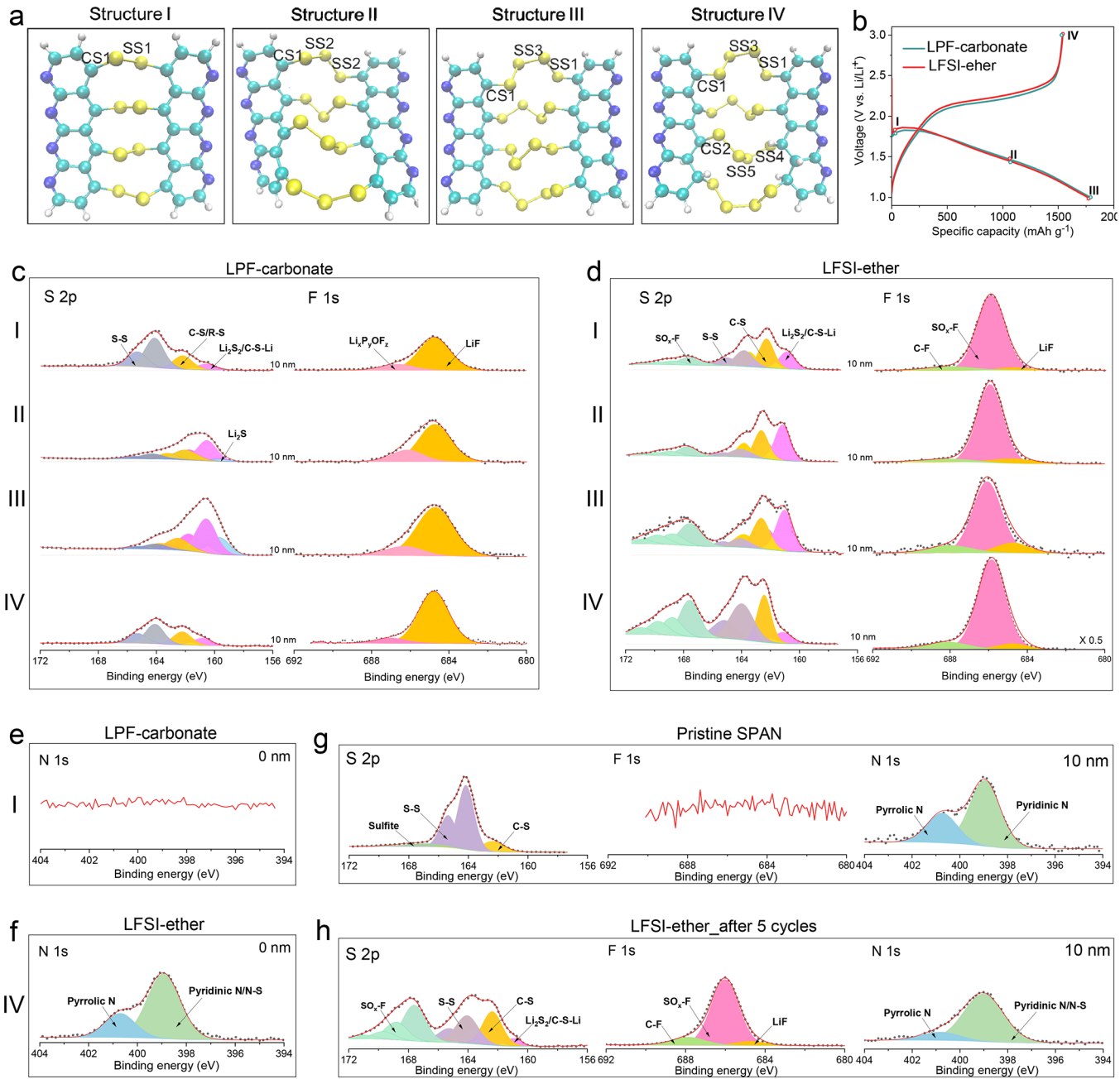

Figure 3. (a) SPAN models with two PAN chains cross-linked by S−S bond (Structure I), S−S−S bond (Structure II), S−S−S−S bond (Structure III), and S−S−S−S bond with four H atoms added to the C atoms which connect to S atoms (Structure IV) for DFT calculations. Color code: C atom, cyan; H atom, white; S atom, yellow; N atom, dark blue. (b) The initial discharge/charge profiles of Li||SPAN cells with different electrolytes at C/10 rate. Sampling points (I, II, III, and IV) for XPS characterizations are marked with dots and numbers. (c, d) S 2p and F 1s XPS spectra collected on the surfaces of SPAN cathodes at different discharge states (points I, II, and III) and charge state (point IV) in (c) LPF-carbonate and (d) LFSI-ether electrolytes, respectively. (e, f) N 1s XPS spectra at signal depth of 0 nm for SPAN (e) at point I in LPF-carbonate and (f) at point IV in LFSI-ether. (g, h) S 2p, F 1s, and N 1s XPS spectra collected on the surfaces of (g) pristine SPAN and (h) SPAN after 5 cycles in LFSI-ether (Signal depth = 10 nm).

LPF-carbonate electrolytes with LPSs are verified through dissolution tests by mixing Li_2S_6 with different solvents and electrolytes. As shown in Figure 1a, the supernatants in pure DME, DME/TTE mixture, and LPF-carbonate turn from colorless to dark-brown, brown and light-brown, respectively, after stirring for 12 h inside an argon-filled glovebox. It suggests that LPSs can dissolve readily in ether solvent DME and be partially soluble in LPF-carbonate. While for pure TTE, it shows zero dissolvability of LPSs as indicated by the colorless supernatant. TTE is a nonsolvating solvent,[34] thus contributing to the unique solvation structure of LFSI-ether as presented in Figure 1b, *i.e.*, highly concentrated salt-solvent clusters surrounded by TTE molecules. This on one hand leads to limited or no free DME molecules in the electrolyte, on the other hand the abundant TTE molecules can act like a shield to prevent the contact between LPSs and DME. Therefore, the LFSI-ether exhibits definite inhibition of LPSs dissolution as supported by the colorless and transparent supernatant after stirring Li_2S_6 in LFSI-ether for 12 h (Figure 1a).

https://doi.org/10.1021/acsami.2c16890
ACS Appl. Mater. Interfaces 2022, 14, 52046−52057

The electrochemical compatibilities of LFSI-ether with SPAN cathode and Li metal anode were examined with a high loading SPAN of ∼11.0 mg cm^{-2}, which is among the highest loading values in previous reports (Table S1). As shown in Figure 1c, the cell in LFSI-ether maintains a capacity retention of 86.9% after 400 cycles under 25 °C, with an average Coulombic efficiency (CE) of ∼100% (Figure 1c) and negligible discharge voltage decay (Figure S1) during the 400 cycles. These merits brought by LFSI-ether are further confirmed by the 84.0% capacity retention after 60 cycles under more practical conditions with 50 μm Li metal anode and 13 μL of electrolyte (Figure S2), and the high capacity retention of 92.1% after 100 cycles under 60 °C (Figure 1d). In contrast, although LPF-carbonate enables higher capacities during both the formation and the following cycles than LFSI-ether, they suffer from rapid capacity drops after only ∼15 cycles when cycling under 25 °C (Figure 1c) and ∼10 cycles when under 60 °C (Figure 1d). These terrible cycling performances are contrary to the previously reported long-term cycling stabilities in carbonate-based electrolytes (Table S1) which benefit from the low SPAN loading (≤2.0 mg cm^{-2}). The observations in LPF-carbonate adequately emphasize the significant influence of cathode loading on the cycling stability of Li||SPAN cells. HT discharge rate performance in Figure 1e suggests that LFSI-ether enables much better rate capability than LPF-carbonate. When discharging at LT (Figures 1f and 1g), LFSI-ether can permit higher capacity retentions, larger average voltage outputs and better capacity recovery ability than LPF-carbonate, and only 2.0% capacity is lost when the temperature backs to 25 °C. It is noted that the two electrolytes suffer sudden voltage drops at −20 and −30 °C, but which are much milder in LFSI-ether. This is mainly due to the serious polarization and can be attributed to two reasons: (1) the significantly increased electrolyte viscosity compared to that at −10 °C, which will lead to further lower Li^+ conductivity and (2) the more sluggish Li^+ ions diffusion in SPAN electrode. These will lead to poor Li^+ ion kinetics during charging/discharging and large overpotential, resulting in the sudden voltage drop under such low temperatures. These observations suggest that the CEI layers generated in LFSI-ether should be more conductive than those in LPF-carbonate, thus benefiting superior Li^+ transfer kinetic.[35] These are further supported by the limited impedance changes even after 400 cycles and the much lower surface film resistance after different cycles in LFSI-ether (Figure S3).

When the cells were disassembled after 100 cycles at 25 °C, it was found that both the SPAN cathode and the Li metal anode cycled in LPF-carbonate were broken into pieces, while those cycled in LFSI-ether still maintained integrity (Figure 2a). Scanning electron microscopy (SEM) images in Figure 2b show that the Li metal anode cycled in LPF-carbonate suffers from an extremely serious corrosion, with a thickness of 455 μm after 100 cycles, twice of the pristine Li thickness of 228 μm. This big thickness or volume change in Li anode side will cause a large pressure on the porous SPAN cathode (which has a high porosity of about 50%), leading to damage like deformation and broken of the laminate. Contrarily, these negative effects at Li metal anode and SPAN cathode are much less severe in LFSI-ether electrolyte. The different effects of the studied electrolytes on Li metal anode and SPAN cathode together determine the divergent cell performance as indicated in Figure 1. Energy dispersive spectroscopy (EDS) (Figures 2c and S4) further suggests the thick surface layer covered on SPAN cycled in LPF-carbonate contains F, P and high weight ratio of O, indicating the significant decompositions of $LiPF_6$ salt and carbonate solvents during cycling. It is speculated that there are constantly serious side reactions on both SPAN cathode and Li metal anode surfaces during the cycling in LPF-carbonate, leading to flimsy surface layers and thus the electrodes break easily after long-term cycles. For SPAN cycled in LFSI-ether, there is no obvious surface layer but the EDS results still show F signal and increased O content compared with pristine SPAN (Figure 2), indicating the decompositions of LiFSI salt and/or TTE diluent (for F) as well as DME solvent and/or TTE (for O) in LFSI-ether electrolyte.

CEI Formation in the Initial Cycles. For a deep insight into the beneficial effect of the LFSI-ether electrolyte on stabilizing the high loading SPAN, the initial CEI formation process is carefully investigated through the combination of ex situ XPS characterization, DFT and AIMD simulation. Since the lithiation process and products of SPAN greatly depend on the structures, DFT and AIMD simulations based on seven SPAN models are first employed to study the lithiation mechanism of SPAN (Figures S5−S12 and related discussions). DFT calculations based on the four structures in Figure 3a show that, the S−S bond lengths in structures I−IV (2.04−2.12 Å) are all larger than the C−S bond lengths (1.79−1.86 Å), When the two PAN chains are cross-linked by S−S−S−S bonds (structure III), it is found that the center S−S bond, *i.e.*, SS3 bond (2.04 Å), is shorter than the S−S bond (SS1) at the edge (2.12 Å). That means the SS1 bond in structure III and SS1 and SS4 bonds in structure IV are easier to be cleaved, which will generate C−S−Li and Li_2S_2 as the lithiation product as well as S_x^{2-} anion or radical for longer polysulfide chain connector. Further AIMD simulations with four types of cross-linked SPAN structures (Figure S5) reveal that the S−S breakage in SPAN is very fast and the bonding between Li and S is also rapid during the lithiation (see the radial distribution functions (RDFs) of S−S and Li−S in Figures S10 and S11, respectively), which are independent with the structures of SPAN. Moreover, as suggested by the observation in RDFs of C−S (Figure S8), a small proportion of the C−S bonds also can be cleaved. This will result in a certain amount of Li_2S_x ($x > 2$) even for structure V, which is probably the reason for the LPSs dissolution in SPAN with ether-based electrolytes in previous reports. And the Li−S reaction rate will mainly depend on the diffusion rate of Li^+ through the CEI layer and in the bulk SPAN. Consequently, the conductivity of CEI layer will become a critical determinant for the electrochemical performance of Li||SPAN cells.

The above calculation results agree well with the following XPS observations. As shown in Figure 3b−3h, the surfaces of SPAN cathodes at three discharge states (Points I, II, and III), after the first cycle (Point IV), and after 5 cycles, are examined through ex situ XPS. At point I, the lithiation product Li_2S_2/C−S−Li species (∼161.6 eV) can obviously be detected on SPAN surfaces in both LPF-carbonate (Figures 3c and S13) and LFSI-ether (Figures 3d and S14). It accompanies with the remarkably decreased intensity ratios (IRs) of S−S signals (∼164.0 eV) to C−S signals (∼162.2 eV) in S 2p spectra ($IR_{S-S/C-S}$) compared to that in pristine SPAN ($IR_{S-S/C-S}$ = 4.34, Figures 3g and S15). Moreover, the much lower $IR_{S-S/C-S}$ in LFSI-ether (0.66) than that in LPF-carbonate (2.17) implies the higher ratio of S−S breakage in LFSI-ether, which should be contributed by the better Li^+ diffusion kinetic

https://doi.org/10.1021/acsami.2c16890
ACS Appl. Mater. Interfaces 2022, 14, 52046−52057

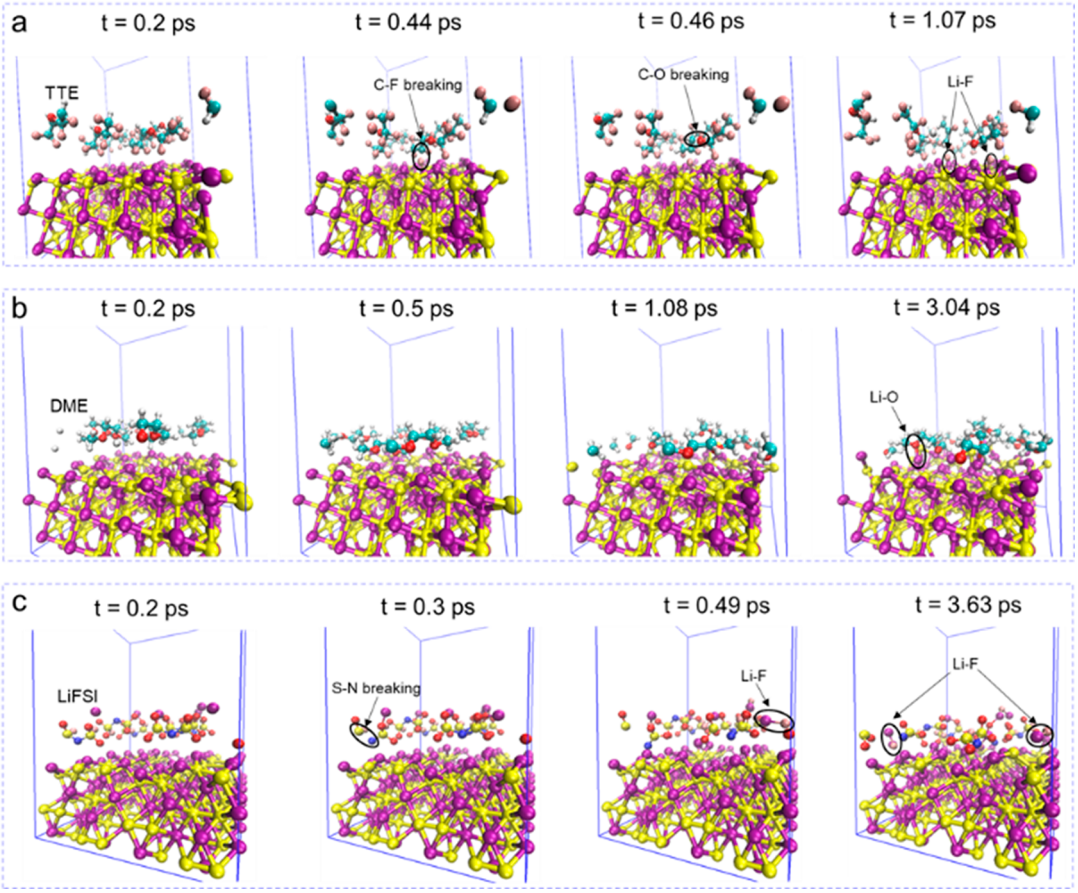

Figure 4. AIMD simulation snapshots of the electrolyte reactivity on Li_2S_2 surface at different periods of time: (a) TTE, (b) DME, and (c) LFSI. Color code: C, cyan; H, white; O, red; F, pink; Li, purple; S, yellow.

benefiting from a conductive CEI layer on SPAN cycled in LFSI-ether. At Points II and III, the peak intensity of Li_2S_2/C−S−Li becomes stronger due to the further lithiation and the $IR_{S-S/C-S}$ gradually decreases in all profiling depths from 0 to 30 nm in the two studied electrolytes (S 2p spectra in Figures 3c, 3d and S16−19). When it comes to Point IV, *i.e.*, after one complete lithiation/delithiation cycle, the S−S signal becomes dominant again due to the breakage of Li−S bonds (Figure S11) and the rebonding among S atoms (Figure S10) but can hardly recover to the state as in the pristine SPAN (Figure S20). This is because some Li atoms are still bonded to S, N and C atoms after the first cycle, as indicated by the existence of Li−S (Figure S11), Li−N (Figure S21), and Li−C (Figure S22) peaks after 20 ps in the RDFs of Li and S, N, and C atoms, respectively, at different periods of time during charge.

For LPF-carbonate, as shown in Figure 3b, at point I, the lithiation process is in its infancy but significant LiF signals (~684.7 eV) can be detected on SPAN, together with obvious $Li_xPO_yF_z$ signal at ~685.6 eV (Figures 3c and S13), indicating the decomposition of $LiPF_6$ salt. Also, solvents decomposition in LPF-carbonate at Point I is demonstrated by the C−O and CO_3^{2-} signals observed in both C 1s (~286.2 and ~290.1 eV, respectively, Figure S23) and O 1s (~531.8 and ~533.7 eV, respectively, Figure S24) XPS spectra. These observations suggest that both the salt and solvent decompositions can be easily initiated and a CEI layer can be formed on the SPAN surface in LPF-carbonate. It is further supported by the absent of N signal at profiling depth of 0 nm (Figure 3e) and the similar N 1s spectra at profiling depths of 10−30 nm (Figure S13) to those of pristine SPAN (Figure S15). Similar observations in F 1s, C 1s, O 1s, and N 1s spectra at Points II, III, and IV further confirm the continuous decomposition of LPF-carbonate during the first cycle (Figures 3c, S16−17, and S20, respectively). Here, it is noted that N 1s signals are absent at 0 nm during the whole discharge/charge cycle in LPF-carbonate, indicating that the surface of SPAN is covered by a thin CEI layer, and the simultaneous appearance of F and N signals at 10−30 nm profiling depths indicates that the electrolyte decomposition products can diffuse into the SPAN bulk.

For LFSI-ether, LiF is a signature of LiFSI salt decomposition but also can be from the TTE diluent. From the F 1s spectra in Figures 3d, S14, and S18−19, only limited LiF signals are detected in SPAN during the whole lithiation process (Points I, II, and III). And, it is surprising to find that the LiF signals are still very limited after the first (Point IV, Figures 3d and S25) and even five discharge/charge cycles (Figures 3h and S26). These observations are very different from the previous results using similar ether-based electrolyte, in which LiF species from LiFSI decomposition can be obviously detected after three formation cycles.[36] In addition, Li_2S, characteristics of LiFSI deep decomposition, is also hardly observed in the S 2p spectra and the N 1s spectra are similar to those of pristine ones. However, significant SO_2−F signals are detected in F 1s spectra at ~686 eV and S 2p spectra at ~167.5/168.7 eV and ~169.3/170.5 eV, which are definitely from the LiFSI salt. It is speculated that the LiFSI salt in LFSI-ether electrolyte shows no significant decom-

https://doi.org/10.1021/acsami.2c16890
ACS Appl. Mater. Interfaces 2022, 14, 52046−52057

position but just suffers a breakage of S−N bonds to form SO_2F and/or N-SO_2F. This agrees well with our recent work, in which it is found that the S−N bond will break first when the FSI^- anion is oxidized and the primary decomposition products of FSI^- anion in CEI are SO_2F (or N-SO_2 F).[37] This is also consistent with the previous report that, in the FSI^- anion structure, the N−S bond is the weakest bond (192.7 kJ mol^{-1}), while the F−S bond is much stronger (652.3 kJ mol^{-1}), indicating that the FSI^- anion could prefer to decompose to form the fragments of SO_2F and/or N-SO_2F.[38] The limited LiF species is more likely from the decomposition of TTE or the reaction between TTE and active lithiation product Li_2S_2, which will be discussed in following sections.

The Origin of CEI Formation. From the above discussion, it is obvious that a CEI layer can be rapidly formed at the preliminary stage of lithiation process in LPF-carbonate. One possible reason is its relatively high cathodic reduction potential starting at ∼1.5 V vs Li/Li^+ with the peak at ∼0.8 V as shown in Figure S27. Another reason is probably related to the side reactions between the electrolyte and the lithiation products of SPAN. In Li||SPAN cells, Li_2S_2 is revealed to be the main active lithiation product of SPAN according to the simulation results. Assary et al. calculated that the reaction rate constant for the C−O bond cleavage by nucleophilic reaction of propylene carbonate (PC) and polysulfides is between 0.93 to 1.59 s^{-1}, which indicates the reaction between PC and polysulfides, especially Li_2S_2 and Li_2S_3, is very easy.[39] The nucleophilic attack of S_2^{2-} with PC can lead to the formation of linear carbonates with C−S bonds. In LPF-carbonate, all solvents, EC, EMC and VC have C═O and C−O bonds like PC has. Therefore, the chemical reactions between Li_2S_2 and EC/EMC/VC solvents during lithiation should be similar to PC reaction. This is supported by the higher binding energy of C−S peaks in lithiated SPAN (∼162.3 eV, Figure 3c) compared to the pristine one (∼161.7 eV, Figure 3g) and the slightly increased ratios of C−S peaks in S 2p spectra with lithiation. Such nucleophilic reaction and the corresponding reaction intermediates are speculated to induce the decompositions of solvents, therefore contributing to the growth of early induced CEI layer on SPAN surface in LPF-carbonate. For LFSI-ether, its electrochemical oxidation stability potential is revealed to be ∼4.4 V,[35,36,40] and the cathodic reduction potential starts at ∼1.5 V and peaked at ∼1.4 V (Figure S27), indicating that LFSI-ether will not be oxidized on SPAN at 3.0 V during charging but it will be reduced on SPAN at 1.0 V at discharging. However, the undetectable CEI layer may suggest other reasons. Moreover, the appearance of LiF species is speculated to relate to the reactions between the LFSI-ether electrolyte and Li_2S_2, which will be discussed in the next section.

LFSI-Ether/Li_2S_2 Reactions. TTE is a kind of hydrofluoroether. It is suggested that such substitution of F atom has a negative influence in terms of the C−O bond stability in the nonfluorinated ether. Since the reacting activation enthalpy of C−F bond is lower than that of C−O bond for beta-F substituted ether,[41] it is expected that some C−F bonds on the TTE molecule will be attacked by Li_2S_2, generating F-containing species in the CEI on SPAN surface during discharge. These are supported by the AIMD simulations of the reactivity of TTE on Li_2S_2 surface (Figure 4a). Initially, all the TTE molecules are a bit far away from the Li_2S_2 surface at t = 0.2 ps, then the TTE molecules move close to the Li_2S_2 surface by the F−Li interaction. At t = 0.44 ps, a C−F bond in a TTE molecule is breaking. At t = 0.46 ps, the C−O bond in a TTE molecule is broken. At t = 1.07 ps, LiF resulting from the reaction between TTE and Li_2S_2 can be observed. These observations indicate that TTE is highly reactive to Li_2S_2 and the reaction rate is fast. However, the molecule size of TTE is large, making the diffusion of TTE molecule into and inside the SPAN electrode relatively difficult and subsequently the diffusion rate is slow. Therefore, the C−F signals are more obvious near the SPAN electrode surface than those in deeper places (for example, F 1s spectra from 0 to 30 nm in Figures 3c and S25), while only limited LiF is observed during the initial cycles (Figures 3d and 3h).

In LFSI-ether electrolyte, DME solvent also has C−O bonds, but it is binding to Li ion, which makes the attack to C−O bond difficult. Figure 4b shows the simulation snapshot of DME/Li_2S_2 reactions at different periods of time. It is found that the DME molecules are a bit far away from the Li_2S_2 surface initially (t = 0.2 ps) and then move to the Li_2S_2 surface slowly. At t = 1.08 ps, when the DME has been very close to the Li_2S_2 surface, its conformation is changed by rotating. When t = 3.04 ps, the binding between Li in Li_2S_2 and O in DME molecule is observed, but the bond cleavage of DME molecule is absent. This implies that the reactivity of DME to Li_2S_2 is lower than TTE and the reaction rate will be slower too. Moreover, in LFSI-ether, LiFSI and DME form clusters that are surround by TTE molecules, making the reactions between DME and Li_2S_2 more difficult. This is beneficial to suppressing the DME decomposition.

For the reactions between LiFSI salt and Li_2S_2, as shown in Figure 4c, the S−N bond in SPAN can be broken by N−Li interaction at t = 0.3 ps. And Li−F bond formation can be observed at t = 0.49 ps, with the amount of which increases over time. It indicates that the reaction between Li_2S_2 and FSI anion is also fast, but the amount of LiF in CEI would depend on the amounts of both FSI^- and Li_2S_2. However, as reported by Jia et al., the dissociation degree of LiFSI in 1.44 M LiFSI in 1.4TMP_a-3TTE was 10.6%, meaning that the LiFSI molecules predominantly exist as Li^+-FSI^- ion pairs in the ion clusters, and the amount of free FSI^- anion is very limited.[42] Similarly, during lithiation process of SPAN in LFSI-ether, the FSI^- ions on SPAN surface is limited and usually exist as Li^+-$Anion^-$-Solvent clusters surrounding by TTE, making the reaction between LiFSI salt and Li_2S_2 difficult. Therefore, the LiF signals detected on SPAN surface even after 5 cycles (Figure 3h) is still limited. While, after longer cycles, with the reaction time accumulates, it is postulated that the possibility of LiFSI/Li_2S_2 reaction increases and considerable amount of LiF could deposit on the SPAN surface.

As discussed above, it is revealed that the attack of Li_2S_2 to DME is difficult. The low reactivity of DME to Li_2S_2 will be beneficial to suppressing solvent decomposition and forming a less organic CEI layer. In contrast, the reactivity of TTE to Li_2S_2 is pretty higher, leading to the formation of LiF on the surface of SPAN cathode. Also, the reaction between LiFSI and Li_2S_2 is rapid. With cycling, the amounts of TTE and LiFSI attacked by Li_2S_2 accumulate, which leads to a LiF-rich CEI layer on SPAN surface.

CEI Layer after Long Cycles. To further figure out the possibility of CEI formation in LFSI-ether, SPAN cathodes after 100 cycles in Li||SPAN cells were taken for XPS depth profiling analyses. XPS analyses on Li metal anodes cycled in LFSI-ether and LPF-carbonate and detail discussions are also provided in Supporting Information (Figures S28−S34) to

https://doi.org/10.1021/acsami.2c16890
ACS Appl. Mater. Interfaces 2022, 14, 52046−52057

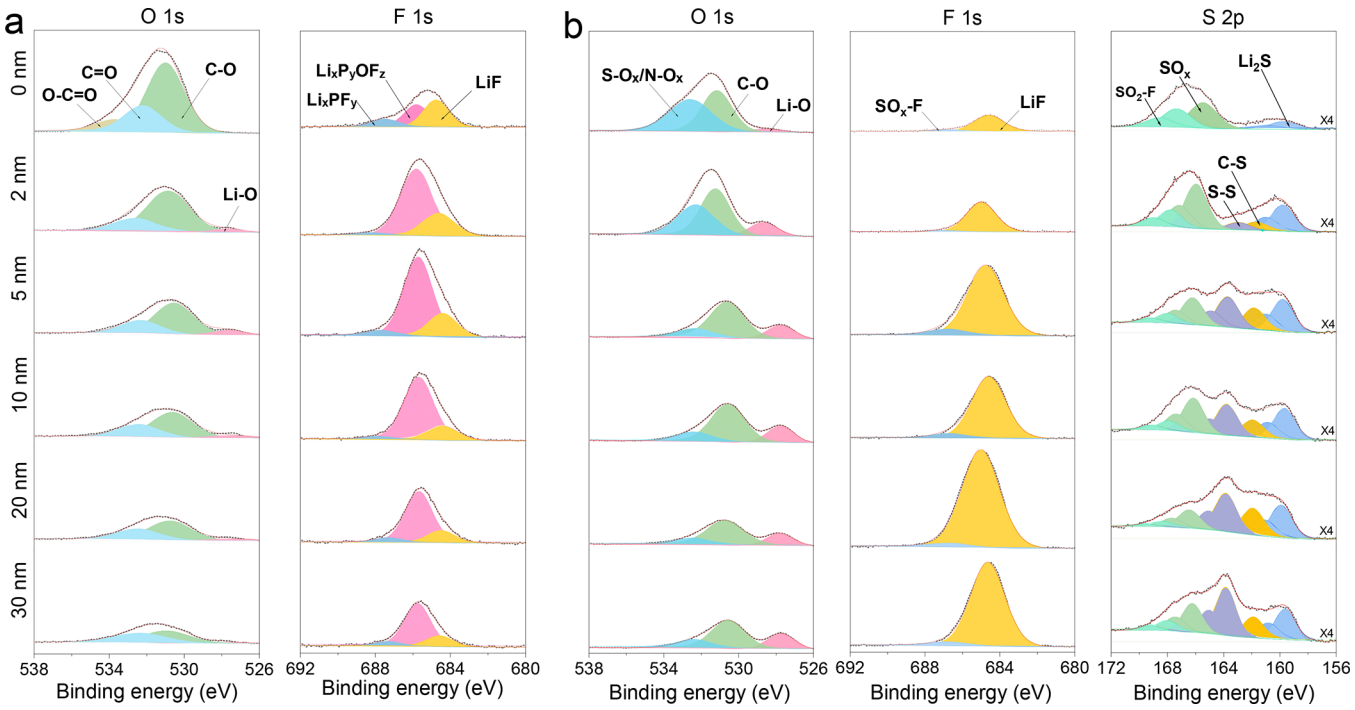

Figure 5. XPS characterization of the electrode/electrolyte interphase components on SPAN cathodes after 100 cycles. O 1s, F 1s, and S 2p XPS depth profiles of the SPAN cathodes cycled in (a) LPF-carbonate and (b) LFSI-ether.

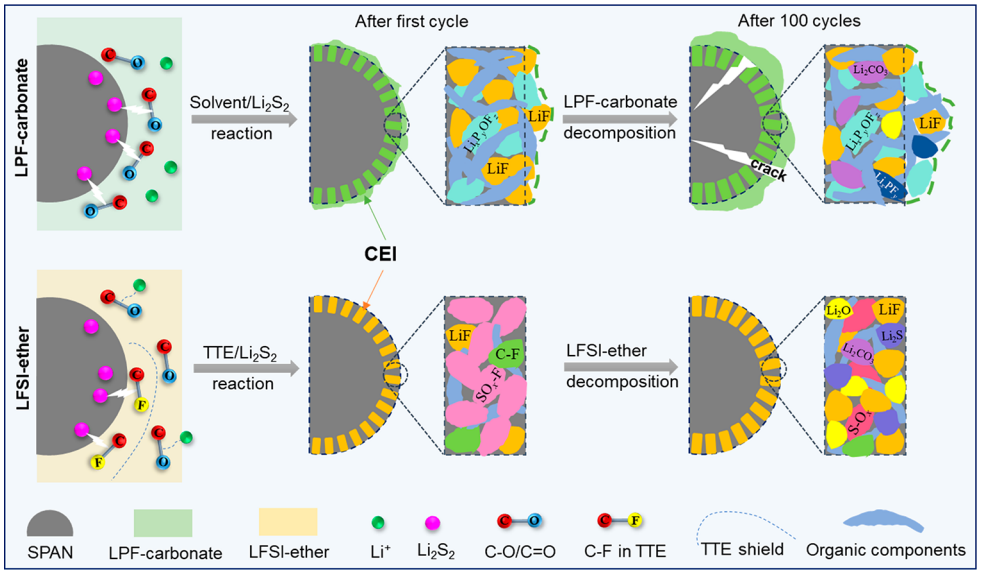

Figure 6. Diagram of CEI formation mechanism and process for SPAN in LPF-carbonate and LFSI-ether electrolytes.

identify the difference of the electrode/electrolyte interphase layers formed in the two electrolytes. Figure 5 shows the O 1s and F 1s XPS spectra of SPAN cathodes cycled in LPF-carbonate and LFSI-ether. For LPF-carbonate, the obvious Li−F signals in F 1s spectra and C−O and C═O signals in O 1s spectra in the profiling depths from 0 to 30 nm suggest the decomposition of salt and solvents, respectively, further demonstrating the formation of CEI layer in LPF-carbonate electrolyte. In addition, the absence of N and S signals in the profiling depths of 0 and 2 nm and the appearance in depths of 5−30 nm indicate the CEI layer enabled by LPF-carbonate is not only formed on the surface of the SPAN cathode but also across it and to the interior (Figures S29).

For LFSI-ether, since SPAN cathode is composed of SPAN composites, conduct carbon and carboxy methylcellulose (CMC) binder, F will be only from the LiFSI salt and the TTE diluent in LillSPAN cells. As discussed above, TTE can react with Li_2S_2 and deliver LiF product. Therefore, the LiF species detected on the SPAN surface as shown in Figure 5b should be from both LFSI and TTE. Strong Li−F signals in F 1s XPS spectra in all the profiling depths on cycled Li metal anode surface can also be observed (Figure S33), further confirming the salt decomposition in LFSI-ether. Furthermore, though the S 2p and N 1s spectra of SPAN after 5 cycles (Figure 3h) are similar to the pristine SPAN, after 100 cycles they are significantly different (Figures 5b and S30). The high

https://doi.org/10.1021/acsami.2c16890
ACS Appl. Mater. Interfaces 2022, 14, 52046−52057

intensity of S^{2-} and SO_xF_y species, together with the obvious $N-O_x$ signals, demonstrates the decomposition of LiFSI. And it is found that C−S and S−S signals from the bulk SPAN can also be observed in depth from 0 to 30 nm. This implies that, rather than forming a CEI layer on the surface of SPAN as most reported, the CEI layer formed in LFSI-ether is pinned into the SPAN. Such a pinning layer in SPAN can not only reduce the porous area thus lowering the electrolyte side reactions, but also strengthen the SPAN structure. This could contribute to the SPAN electrode integrity after 100 cycles (Figure 2a). Moreover, unlike the XPS observation in the initial cycles, C−O signals (O 1s XPS spectra in Figure 5b) and C−F signals (C 1s XPS spectra in Figure S30) can be detected in different depths, suggesting the decomposition of DME and TTE molecules in LFSI-ether. Beltran et al. have studied the interfacial reactivity of DOL, DMC, and EC with lithiated SPAN via AIMD simulations.[43] They demonstrated that both DOL and DMC are pretty stable on SPAN surface during multiple stages of lithiation, and EC is only reduced in an overdischarge regime with voltages close to 0 V vs Li/Li^+. In this work, the LFSI-ether has a unique solvation structure as indicated in Figure 1b, and the salt, solvent and diluent can react with the lithiation product of SPAN (Figure 4), which could temporarily change the solvation structure, leading to different decomposition mechanism from that in high-voltage battery system like Li||NMC. All of these contribute to the formation of LiF-rich CEI layer on SPAN and result in the superior cell performance in LFSI-ether electrolyte for Li|| SPAN cell with a high loading SPAN cathode.

Based on the above discussions, the origin and process of CEI formation on SPAN with LPF-carbonate and LFSI-ether electrolytes, respectively, are summarized in Figure 6. For LPF-carbonate, it is revealed that the nucleophilic reaction between C−O/C═O and Li_2S_2 can induce the solvent decomposition and subsequently $LiPF_6$ decomposition, therefore contributing to the growth of early induced CEI layer on both the out surface and the internal surface of SPAN. After the first cycle, the CEI layer is dominated by LiF and organic species. After 100 cycles, the CEI layer accumulated on the out surface of SPAN becomes thicker, and the components are mainly organic species, accompanying with limited inorganic species like LiF, Li_2O, and Li_2CO_3. In LFSI-ether, DME binds to Li^+ and is surrounded by TTE, making the C−O on DME hardly be attacked by Li_2S_2. Therefore, DME decomposition is suppressed, consequently reducing the amount of organic species in CEI. Although LiFSI is hardly decomposed via electrochemical reduction at 1.0 V or electrochemical oxidation under low voltage of 3.0 V, the high reactivity of Li_2S_2 to C−F bonds of TTE leads to the decomposition of TTE and the formation of LiF, and the reaction between LiFSI and Li_2S_2 results in the breakage of S−N bond and the generation of SO_x-F species. However, the size of TTE molecules is usually large and it is hard for them to diffuse into SPAN to react with Li_2S_2. Therefore, after the first cycle, the CEI layer formed in LFSI-ether is dominated by SO_x-F species, accompanying with limited LiF. And it is noted that the CEI formed in LFSI-ether pins in the SPAN bulk like nails, which is supposed to benefit the strength of SPAN. With cycling, the products from TTE/Li_2S_2 and LiFSI/Li_2S_2 reactions accumulate, and the solvation structure of LFSI-ether is gradually changed, leading to the decomposition of the salt and diluent. After 100 cycles, the CEI keeps growing inward rather than to the out surface of SPAN, and riches with inorganic species, especially LiF. Besides the difference in passivation ability and Li^+ ion conductivity for organic-rich and inorganic-rich CEI layers, the swelling properties will be also different. Being enriched with organic compounds, the CEI layer in LPF-carbonate would be easily swollen by the electrolyte. For the CEI layer in LFSI-ether, it is rich in inorganic compounds, which is hardly swollen by the electrolyte. Under the combination of these differences in CEI properties, the cell performances in the two studied electrolytes exhibit obvious contrasts.

CONCLUSION

In this work, the Li storage mechanism and the original formation processes of CEI layers for SPAN in carbonated-based and ether-based electrolytes are well understood through computational simulations and experimental investigation. First, Li_2S_2 is revealed to be the main active product of lithiation in SPAN and the Li^+ trapped by Li−S, Li−N, and Li−C bonds are the main contribution of irreversible capacity loss in the first cycle for Li||SPAN batteries, being regardless of the electrolyte system. Second, the reactions between Li_2S_2 and C−O/C═O in LPF-carbonate or C−F of TTE and N−S of LiFSI in LSI-ether initiate the growth of a CEI layer. In LPF-carbonate, the dominated solvent decomposition in the initial cycle leads to the formation of CEI on the inner and outer layers of the SPAN surface. In LFSI-ether, the suppressed DME decomposition but dominated LiFSI decomposition result in less organic species which have large molecule size. Thus, the CEI formed in LFSI-ether can fill into the SPAN bulk and strengthen SPAN like pinning layer. Third, the CEI layer formed in LFSI-ether is demonstrated to be conductive, robust and thin, leading to long-term cycling stability with high S loading under both room and high temperature, fast discharge capability and superior LT performance. These deep understandings of the origin of electrode/electrolyte interphase formation in different electrolyte systems will facilitate the coming studies on precise electrolyte design toward future high-energy density Li-sulfur applications.

ASSOCIATED CONTENT

Supporting Information

The Supporting Information is available free of charge at https://pubs.acs.org/doi/10.1021/acsami.2c16890.

AIMD and DFT data and XPS details, as well as related discussions, Figures S1−S34, and Tables S1 and S2 (PDF)

AUTHOR INFORMATION

Corresponding Authors

Ping Liu − *Department of NanoEngineering and Sustainable Power and Energy Center, University of California San Diego, La Jolla, California 92093, United States;* orcid.org/0000-0002-1488-1668; Email: piliu@ucsd.edu

Wu Xu − *Energy and Environment Directorate, Pacific Northwest National Laboratory, Richland, Washington 99354, United States;* orcid.org/0000-0002-2685-8684; Email: wu.xu@pnnl.gov

Authors

Xianhui Zhang − *Energy and Environment Directorate, Pacific Northwest National Laboratory, Richland, Washington 99354, United States;* orcid.org/0000-0001-5992-9269

Peiyuan Gao − *Physical and Computational Sciences Directorate, Pacific Northwest National Laboratory, Richland, Washington 99354, United States;* orcid.org/0000-0002-2906-6551

Zhaohui Wu − *Department of NanoEngineering, University of California San Diego, La Jolla, California 92093, United States*

Mark H. Engelhard − *Environmental Molecular Sciences Laboratory, Pacific Northwest National Laboratory, Richland, Washington 99354, United States;* orcid.org/0000-0002-5543-0812

Xia Cao − *Energy and Environment Directorate, Pacific Northwest National Laboratory, Richland, Washington 99354, United States*

Hao Jia − *Energy and Environment Directorate, Pacific Northwest National Laboratory, Richland, Washington 99354, United States;* orcid.org/0000-0003-2814-5589

Yaobin Xu − *Environmental Molecular Sciences Laboratory, Pacific Northwest National Laboratory, Richland, Washington 99354, United States;* orcid.org/0000-0002-9945-3514

Haodong Liu − *Department of NanoEngineering, University of California San Diego, La Jolla, California 92093, United States*

Chongming Wang − *Environmental Molecular Sciences Laboratory, Pacific Northwest National Laboratory, Richland, Washington 99354, United States;* orcid.org/0000-0003-3327-0958

Jun Liu − *Energy and Environment Directorate, Pacific Northwest National Laboratory, Richland, Washington 99354, United States; Materials Science and Engineering Department, University of Washington, Seattle, Washington 98195, United States;* orcid.org/0000-0001-8663-7771

Ji-Guang Zhang − *Energy and Environment Directorate, Pacific Northwest National Laboratory, Richland, Washington 99354, United States;* orcid.org/0000-0001-7343-4609

Complete contact information is available at: https://pubs.acs.org/10.1021/acsami.2c16890

Author Contributions

‡X.Z. and P.G. contributed equally. The manuscript was written through contributions of all authors. All authors have given approval to the final version of the manuscript.

Notes

The authors declare no competing financial interest.

■ ACKNOWLEDGMENTS

This work was supported by the Assistant Secretary for Energy Efficiency and Renewable Energy, Vehicle Technologies Office, of the U.S. Department of Energy (DOE) through the Advanced Battery Materials Research program (Battery500 Consortium) under the contract no. DE-AC05-76RL01830. The XPS characterization was supported under a partial grant from the Washington State Department of Commerce's Clean Energy Fund and performed at the Environmental Molecular Sciences Laboratory, a DOE Office of Science User Facility sponsored by the Office of Biological and Environmental Research and located at Pacific Northwest National Laboratory (PNNL). PNNL is operated by Battelle for the DOE under Contract DE-AC05-76RL01830. The LiFSI salt was provided by Dr. Kazuhiko Murata of Nippon Shokubai Co., Ltd.

■ REFERENCES

(1) Pang, Q.; Shyamsunder, A.; Narayanan, B.; Kwok, C. Y.; Curtiss, L. A.; Nazar, L. F. Tuning the Electrolyte Network Structure to Invoke Quasi-Solid State Sulfur Conversion and Suppress Lithium Dendrite Formation in Li−S Batteries. *Nat. Energy* **2018**, *3* (9), 783−791.

(2) Cheng, X. B.; Zhang, R.; Zhao, C. Z.; Zhang, Q. Toward Safe Lithium Metal Anode in Rechargeable Batteries: A Review. *Chem. Rev.* **2017**, *117* (15), 10403−10473.

(3) Li, Z.; Zhang, J.; Lu, Y.; Lou, X. A Pyrolyzed Polyacrylonitrile/Selenium Disulfide Composite Cathode with Remarkable Lithium and Sodium Storage Performances. *Sci. Adv.* **2018**, *4*, 1687−1696.

(4) Pang, Q.; Liang, X.; Kwok, C. Y.; Nazar, L. F. Advances in Lithium−Sulfur Batteries Based on Multifunctional Cathodes and Electrolytes. *Nat. Energy* **2016**, *1* (9), 16132.

(5) Holoubek, J.; Liu, H.; Wu, Z.; Yin, Y.; Xing, X.; Cai, G.; Yu, S.; Zhou, H.; Pascal, T. A.; Chen, Z.; Liu, P. Tailoring Electrolyte Solvation for Li Metal Batteries Cycled at Ultra-Low Temperature. *Nat. Energy* **2021**, *6*, 303−313.

(6) Tan, S.; Liu, H.; Wu, Z.; Weiland, C.; Bak, S. M.; Ronne, A.; Liu, P.; Whittingham, M. S.; Shadike, Z.; Hu, E.; Yang, X. Q. Isoxazole-Based Electrolytes for Lithium Metal Protection and Lithium-Sulfurized Polyacrylonitrile (Span) Battery Operating at Low Temperature. *J. Electrochem. Soc.* **2022**, *169* (3), 030513.

(7) Wei, S.; Ma, L.; Hendrickson, K. E.; Tu, Z.; Archer, L. A. Metal-Sulfur Battery Cathodes Based on Pan-Sulfur Composites. *J. Am. Chem. Soc.* **2015**, *137* (37), 12143−52.

(8) Wang, J.; Lin, F.; Jia, H.; Yang, J.; Monroe, C. W.; NuLi, Y. Towards a Safe Lithium-Sulfur Battery with a Flame-Inhibiting Electrolyte and a Sulfur-Based Composite Cathode. *Angew. Chem.* **2014**, *53* (38), 10099−104.

(9) Lei, J.; Lu, H.; Chen, J.; Yang, J.; Nuli, Y.; Wang, J. Crosslinked Polyacrylonitrile Precursor for S@ Ppan Composite Cathode Materials for Rechargeable Lithium Batteries. *J. Energy Chem.* **2022**, *65*, 186−193.

(10) Zhang, S.; Ren, W.; NuLi, Y.; Wang, B.; Yang, J.; Wang, J. Sulfurized-Pyrolyzed Polyacrylonitrile Cathode for Magnesium-Sulfur Batteries Containing Mg2+/Li+ Hybrid Electrolytes. *Chem. Eng. J.* **2022**, *427*, 130902.

(11) Lei, J.; Chen, J.; Naveed, A.; Zhang, H.; Yang, J.; Nuli, Y.; Wang, J. Sulfurized Polyacrylonitrile Cathode Derived from Intermolecular Cross-Linked Polyacrylonitrile for a Rechargeable Lithium Battery. *ACS Appl. Energy Mater.* **2021**, *4* (6), 5706−5712.

(12) Yang, H.; Naveed, A.; Li, Q.; Guo, C.; Chen, J.; Lei, J.; Yang, J.; Nuli, Y.; Wang, J. Lithium Sulfur Batteries with Compatible Electrolyte Both for Stable Cathode and Dendrite-Free Anode. *Energy Storage Mater.* **2018**, *15*, 299−307.

(13) Warneke, S.; Hintennach, A.; Buchmeiser, M. R. Communication—Influence of Carbonate-Based Electrolyte Composition on Cell Performance of Span-Based Lithium-Sulfur-Batteries. *J. Electrochem. Soc.* **2018**, *165* (10), A2093−A2095.

(14) Wang, X.; Qian, Y.; Wang, L.; Yang, H.; Li, H.; Zhao, Y.; Liu, T. Sulfurized Polyacrylonitrile Cathodes with High Compatibility in Both Ether and Carbonate Electrolytes for Ultrastable Lithium−Sulfur Batteries. *Adv. Funct. Mater.* **2019**, *29* (39), 1902929.

(15) Xu, Z.; Wang, J.; Yang, J.; Miao, X.; Chen, R.; Qian, J.; Miao, R. Enhanced Performance of a Lithium−Sulfur Battery Using a Carbonate-Based Electrolyte. *Angew. chem.* **2016**, *55* (35), 10372−10375.

(16) Chen, S.; Zheng, J.; Yu, L.; Ren, X.; Engelhard, M. H.; Niu, C.; Lee, H.; Xu, W.; Xiao, J.; Liu, J.; Zhang, J.-G. High-Efficiency Lithium Metal Batteries with Fire-Retardant Electrolytes. *Joule* **2018**, *2* (8), 1548−1558.

(17) Fan, X.; Chen, L.; Borodin, O.; Ji, X.; Chen, J.; Hou, S.; Deng, T.; Zheng, J.; Yang, C.; Liou, S. C.; Amine, K.; Xu, K.; Wang, C. Non-Flammable Electrolyte Enables Li-Metal Batteries with Aggressive Cathode Chemistries. *Nat. nanotech.* **2018**, *13* (8), 715−722.

(18) Lee, H.; Lim, H.-S.; Ren, X.; Yu, L.; Engelhard, M. H.; Han, K. S.; Lee, J.; Kim, H.-T.; Xiao, J.; Liu, J.; Xu, W.; Zhang, J.-G.

Detrimental Effects of Chemical Crossover from the Lithium Anode to Cathode in Rechargeable Lithium Metal Batteries. *ACS Energy Lett.* **2018**, *3* (12), 2921−2930.
(19) Chen, J.; Zhang, H.; Yang, H.; Lei, J.; Naveed, A.; Yang, J.; Nuli, Y.; Wang, J. Towards Practical Li−S Battery with Dense and Flexible Electrode Containing Lean Electrolyte. *Energy Storage Mater.* **2020**, *27*, 307−315.
(20) Peng, H.-J.; Huang, J.-Q.; Cheng, X.-B.; Zhang, Q. Review on High-Loading and High-Energy Lithium-Sulfur Batteries. *Adv. Energy Mater.* **2017**, *7* (24), 1700260.
(21) Zhang, Y.; Sun, Y.; Peng, L.; Yang, J.; Jia, H.; Zhang, Z.; Shan, B.; Xie, J. Se as Eutectic Accelerator in Sulfurized Polyacrylonitrile for High Performance All-Solid-State Lithium-Sulfur Battery. *Energy Storage Mater.* **2019**, *21*, 287−296.
(22) Yang, H.; Chen, J.; Yang, J.; Wang, J. Prospect of Sulfurized Pyrolyzed Poly(Acrylonitrile) (S@Ppan) Cathode Materials for Rechargeable Lithium Batteries. *Angew. Chem.* **2020**, *132* (19), 7374−7386.
(23) Xing, X.; Li, Y.; Wang, X.; Petrova, V.; Liu, H.; Liu, P. Cathode Electrolyte Interface Enabling Stable Li−S Batteries. *Energy Storage Mater.* **2019**, *21*, 474−480.
(24) Yang, H.; Chen, J.; Yang, J.; Nuli, Y.; Wang, J. Dense and High Loading Sulfurized Pyrolyzed Poly (Acrylonitrile)(S@Ppan) Cathode for Rechargeable Lithium Batteries. *Energy Storage Mater.* **2020**, *31*, 187−194.
(25) Lei, J.; Chen, J.; Zhang, H.; Naveed, A.; Yang, J.; Nuli, Y.; Wang, J. High Molecular Weight Polyacrylonitrile Precursor for S@ Ppan Composite Cathode Materials with High Specific Capacity for Rechargeable Lithium Batteries. *ACS Appl. Mater. & Interfaces* **2020**, *12* (30), 33702−33709.
(26) Zhang, X.; Zou, L.; Cui, Z.; Jia, H.; Engelhard, M. H.; Matthews, B. E.; Cao, X.; Xie, Q.; Wang, C.; Manthiram, A.; Zhang, J.-G.; Xu, W. Stabilizing Ultrahigh-Nickel Layered Oxide Cathodes for High-Voltage Lithium Metal Batteries. *Mater. Today* **2021**, *44*, 15−24.
(27) Liu, H.; Holoubek, J.; Zhou, H.; Chen, A.; Chang, N.; Wu, Z.; Yu, S.; Yan, Q.; Xing, X.; Li, Y.; Pascal, T. A.; Liu, P. Ultrahigh Coulombic Efficiency Electrolyte Enables Li||Span Batteries with Superior Cycling Performance. *Mater. Today* **2021**, *42*, 17−28.
(28) Wu, Z.; Bak, S. M.; Shadike, Z.; Yu, S.; Hu, E.; Xing, X.; Du, Y.; Yang, X. Q.; Liu, H.; Liu, P. Understanding the Roles of the Electrode/Electrolyte Interface for Enabling Stable Li Parallelsulfurized Polyacrylonitrile Batteries. *ACS Appl. Mater. & Interfaces* **2021**, *13* (27), 31733−31740.
(29) He, Y.; Zou, P.; Bak, S. M.; Wang, C.; Zhang, R.; Yao, L.; Du, Y.; Hu, E.; Lin, R.; Xin, H. L. Dual Passivation of Cathode and Anode through Electrode−Electrolyte Interface Engineering Enables Long-Lifespan Li Metal−Span Batteries. *ACS Energy Lett.* **2022**, *7*, 2866−2875.
(30) Xin, S.; Gu, L.; Zhao, N.-H.; Yin, Y.-X.; Zhou, L.-J.; Guo, Y.-G.; Wan, L.-J. Smaller Sulfur Molecules Promise Better Lithium-Sulfur Batteries. *J. Am. Chem. Soc.* **2012**, *134* (45), 18510−18513.
(31) Chen, X.; Peng, L.; Wang, L.; Yang, J.; Hao, Z.; Xiang, J.; Yuan, K.; Huang, Y.; Shan, B.; Yuan, L.; Xie, J. Ether-Compatible Sulfurized Polyacrylonitrile Cathode with Excellent Performance Enabled by Fast Kinetics Via Selenium Doping. *Nat. comm.* **2019**, *10* (1), 1021.
(32) Dokko, K.; Tachikawa, N.; Yamauchi, K.; Tsuchiya, M.; Yamazaki, A.; Takashima, E.; Park, J.-W.; Ueno, K.; Seki, S.; Serizawa, N.; Watanabe, M. Solvate Ionic Liquid Electrolyte for Li−S Batteries. *J. Electrochem. Soc.* **2013**, *160* (8), A1304−A1310.
(33) Valiev, M.; Bylaska, E. J.; Govind, N.; Kowalski, K.; Straatsma, T. P.; Van Dam, H. J. J.; Wang, D.; Nieplocha, J.; Apra, E.; Windus, T. L.; de Jong, W. A. Nwchem: A Comprehensive and Scalable Open-Source Solution for Large Scale Molecular Simulations. *Comput. Phys. Commun.* **2010**, *181* (9), 1477−1489.
(34) Kresse, G.; Joubert, D. From Ultrasoft Pseudopotentials to the Projector Augmented-Wave Method. *Phys. Rev. B* **1999**, *59* (3), 1758−1775.
(35) Cao, X.; Jia, H.; Xu, W.; Zhang, J.-G. Review—Localized High-Concentration Electrolytes for Lithium Batteries. *J. Electrochem. Soc.* **2021**, *168* (1), 010522.
(36) Zhang, X.; Zou, L.; Xu, Y.; Cao, X.; Engelhard, M. H.; Matthews, B. E.; Zhong, L.; Wu, H.; Jia, H.; Ren, X.; Gao, P.; Chen, Z.; Qin, Y.; Kompella, C.; Arey, B. W.; Li, J.; Wang, D.; Wang, C.; Zhang, J. G.; Xu, W. Advanced Electrolytes for Fast-Charging High-Voltage Lithium-Ion Batteries in Wide-Temperature Range. *Adv. Energy Mater.* **2020**, *10* (22), 2000368.
(37) Jia, H.; Xu, Y.; Burton, S. D.; Gao, P.; Zhang, X.; Matthews, B. E.; Engelhard, M. H.; Zhong, L.; Bowden, M. E.; Xiao, B.; Han, K. S.; Wang, C.; Xu, W. Enabling Ether-Based Electrolytes for Long Cycle Life of Lithium-Ion Batteries at High Charge Voltage. *ACS Appl. Mater. & Interfaces* **2020**, *12* (49), 54893−54903.
(38) Zou, L.; Gao, P.; Jia, H.; Cao, X.; Wu, H.; Wang, H.; Zhao, W.; Matthews, B. E.; Xu, Z.; Li, X.; Zhang, J. G.; Xu, W.; Wang, C. Nonsacrificial Additive for Tuning the Cathode−Electrolyte Interphase of Lithium-Ion Batteries. *ACS Appl. Mater. Interfaces 2022* **2022**, *14* (3), 4111−4118.
(39) Cao, R.; Chen, J.; Han, K. S.; Xu, W.; Mei, D.; Bhattacharya, P.; Engelhard, M. H.; Mueller, K. T.; Liu, J.; Zhang, J.-G. Effect of the Anion Activity on the Stability of Li Metal Anodes in Lithium-Sulfur Batteries. *Adv. Funct. Mater.* **2016**, *26* (18), 3059−3066.
(40) Assary, R. S.; Curtiss, L. A.; Moore, J. S. Toward a Molecular Understanding of Energetics in Li−S Batteries Using Nonaqueous Electrolytes: A High-Level Quantum Chemical Study. *J. Phys. Chem. C* **2014**, *118* (22), 11545−11558.
(41) Ren, X.; Zou, L.; Cao, X.; Engelhard, M. H.; Liu, W.; Burton, S. D.; Lee, H.; Niu, C.; Matthews, B. E.; Zhu, Z.; Wang, C.; Arey, B. W.; Xiao, J.; Liu, J.; Zhang, J.-G.; Xu, W. Enabling High-Voltage Lithium-Metal Batteries under Practical Conditions. *Joule* **2019**, *3* (7), 1662−1676.
(42) Assary, R. S.; Curtiss, L. A. Molecular Level Understanding of the Interactions between Reaction Intermediates of Li−S Energy Storage Systems and Ether Solvents. In *Lithium−Sulfur Batteries*; John Wiley & Sons Ltd., 2019; pp 133−146.
(43) Perez Beltran, S.; Balbuena, P. B. A Solid Electrolyte Interphase to Protect the Sulfurized Polyacrylonitrile (Span) Composite for Li−S Batteries: Computational Approach Addressing the Electrolyte/Span Interfacial Reactivity. *J. Mater. Chem. A* **2021**, *9* (12), 7888−7902.

https://doi.org/10.1021/acsami.2c16890
ACS Appl. Mater. Interfaces 2022, 14, 52046−52057